

Structure and dynamics of Taylor vortex flow and the effect of subcritical driving ramps^{*}

M. Lücke and D. Roth

Institut für Theoretische Physik, Universität des Saarlandes, Saarbrücken,
 Federal Republic of Germany

Received September 11, 1989

Finite difference numerical solutions for rotationally symmetric flows in the rotating Couette system are presented. Axial and radial structures of velocity and pressure of Taylor vortices are elucidated. The Reynolds number dependence of their axial Fourier amplitudes is compared with theory. The wave number selection by ramps realized at constant geometry by slow axial decrease of the driving from super- to subcritical values is determined. The phase dynamics of the response to moving a boundary is compared with theory. The long-time effective phase diffusion constant strongly depends on the axial amplitude profile of the vortex structure.

1. Introduction

The Taylor-Couette problem [1] of fluid flow in the annulus between concentric cylinders with the inner one rotating and the outer one being stationary is one of the simplest examples of driven nonlinear dissipative systems. Upon increasing the driving beyond a critical threshold there is a transition from a subcritically stable stationary homogeneous state to a supercritically stable stationary spatially periodic state. The former is circular Couette flow (CCF). The latter is Taylor vortex flow (TVF), i.e., rotationally symmetric toroidally closed vortices that are axially stacked upon each other with alternating turning directions. What makes TVF appealing for studies of structure formation in driven systems by experimental, analytical, and numerical means alike is the low dimensionality of the structured state: Rotational symmetry of the toroidal vortices reduces the spatial variables to two, the (local) wave vector of the flow pattern showing along the cylinder axes depends at most on the axial variable, and to lowest order in a perturbation expansion [2] around the bifurcation threshold the amplitude of the TVF structure is given by the solu-

tion of a complex one-dimensional Ginzburg-Landau amplitude Eq. (3).

We shall elucidate in some detail the structure of the stationary TVF state [1, 4–19] and the dynamical response behaviour, in particular of its phase [20–23], to certain perturbations. We investigate the effect of slow axial variations – ramps – in the driving. They smoothly connect an upper part of the annulus where with supercritical driving the structured state is fully realized with a subcritical lower part at the end of which the subcritical homogeneous state, here CCF, is enforced. The motivation for studying [24–34, 10, 14] the effect of ramps on dissipative structures is the elimination of boundary phase pinning. A ramp lets the pattern in the supercritical part of the system select a preferred wave-length [25] out of the wide range of wave-lengths which are realizable in unramped systems by compressing or dilating the structure by moving a boundary. It turns out that structural properties of the TVF pattern in the supercritical driving part are not affected by the ramp while the selected narrow band of wave numbers depends [32] on the ramp details.

In Sect. 2 we describe the system and our investigation method. In Sect. 3 we present our results on the structure of TVF. We discuss the radial and axial

^{*} Dedicated to Professor W. Brenig on the occasion of his 60th birthday

variation of all fields, we perform axial Fourier analyses, and we contrast structural properties of Taylor vortices with those of roll vortices in Bénard convection. Section 4 deals with wave number selection by driving ramps. In the final Sect. 5 we investigate the phase dynamics of the TVF pattern in response to moving a boundary position. In particular we determine the long-time relaxation behaviour of the vortex centers to their stationary locations. We reproduce the long-time effective diffusion constants determined from the numerical simulation of the full field equations with the phase equation of the Ginzburg-Landau equation when taking the modulus of the amplitude properly into account. Axial variations of the latter induced by boundary conditions and ramps drastically influence the effective phase diffusion constant.

2. The Taylor-Couette problem

Since the system and our investigation method has been described earlier [11], we give here only a short description to fix the notation.

2.1. The system

We have studied axisymmetric flow of an incompressible fluid in the annulus between two concentric cylinders of inner radius r_1 and outer radius r_2 with a gapwidth $d=r_2-r_1$. The axial extension is $L=\Gamma d$. Typically the aspect ratio Γ was around 25 in our numerical simulations with some control runs made with Γ up to 35. The radius ratio $\eta=r_1/r_2$ was in most cases 0.75 and in some runs 0.893. Always the outer cylinder was at rest and a finite tangential velocity, $v_1(z, t)$, was imposed at the inner cylinder, $r=r_1$. The resulting flow is given by the solution of the continuity equation, $\nabla \cdot \mathbf{u}=0$, and the Navier-Stokes equation (NSE)

$$(\partial_t + \mathbf{u} \cdot \nabla) \mathbf{u} = -\frac{1}{\rho} \nabla p + \nu \nabla^2 \mathbf{u}. \quad (2.1)$$

Here ν is the kinematic viscosity, ρ the constant mass density, p the pressure field, and \mathbf{u} the velocity field. Its radial, azimuthal, and axial components are denoted by u, v, w in a cylindrical coordinate system

$$\mathbf{u} = u \mathbf{e}_r + v \mathbf{e}_\varphi + w \mathbf{e}_z. \quad (2.2)$$

Restricting ourselves to rotational symmetric flows u, v, w, p depend besides on time t only on r, z but not on the azimuthal angle φ .

As control parameter measuring the strength of the driving we take the Reynolds number

$$R = \frac{v_1 d}{\nu}. \quad (2.3)$$

We also introduce the relative control parameter

$$\varepsilon = \frac{R}{R_c} - 1 \quad (2.4)$$

that measures the relative distance from the critical value R_c of the Reynolds number for onset of Taylor vortices. The threshold values $R_c(\eta=0.75)=85.78$ and $R_c(\eta=0.893)=127.34$ result from linear stability analyses [1, 35] done with stationary homogeneous driving v_1 .

For subcritical driving, $R < R_c$, circular Couette flow (CCF)

$$u_{\text{CCF}} = 0 = w_{\text{CCF}};$$

$$v_{\text{CCF}}(r) = v_1 \left[\frac{r_1}{r} - \eta^2 \frac{r}{r_1} \right] \frac{1}{1-\eta^2} \quad (2.5)$$

$$p_{\text{CCF}}(r) = \rho \frac{v_1^2}{2} \left\{ \eta^4 \left[\left(\frac{r}{r_1} \right)^2 - 1 \right] - 4\eta^2 \ln \left(\frac{r}{r_1} \right) + 1 - \left(\frac{r_1}{r} \right)^2 \right\} \left(\frac{1}{1-\eta^2} \right)^2 \quad (2.6)$$

is the stable solution of (2.1) for the infinite system, $\Gamma = \infty$. At threshold, $\varepsilon = 0$, the axially homogeneous CCF state becomes unstable and a stable, stationary, axially periodic, rotationally symmetric TVF state bifurcates out of the CCF solution with an amplitude that increases close to threshold $\sim \sqrt{\varepsilon}$. Henceforth we shall scale lengths by the gapwidth d , times by the momentum diffusion time d^2/ν across the gap, velocity by v/d , and pressure by $\rho v^2/d^2$.

2.2. Numerical simulation

To determine the evolution towards the TVF state and its structure we have solved numerically the time dependent field Eqs. (2.1) in their rotationally symmetric form in an $r-z$ crosssection of the annulus using an explicit finite difference scheme as in [11]. However, in the present calculations the Poisson equation for the pressure was solved by iteratively adjusting at each time step the advanced velocity and the pressure to each other [36] so as to guarantee $\nabla \cdot \mathbf{u} = 0$.

We always imposed at the top end of the annulus, $z = \Gamma$, the boundary condition $\mathbf{u} = 0$ appropriate for a rigid stationary plate in contact with the fluid. That creates (also for subcritical driving) a so-called Ekman

vortex [1] which influences the TVF state further down in the bulk. In particular causes the Ekman vortex below the top plate due to its fixed location and largely undeformable shape a strong phase pinning on the top end of the TVF structure [9, 11, 37, 38]. To avoid a similar pinning of the TVF structure also at the lower end of the annulus we imposed there a slow axial ramp in the Reynolds number. The ramp was realized as a ramp in the driving by an axial variation of the tangential velocity, $v_1(z)$, at r_1 keeping the gap width fixed. The local control parameter $\varepsilon(z)$ starts to drop at $z=12$ from a supercritical value, $\varepsilon > 0$, to a final subcritical value, $\varepsilon(z=0) < 0$, at the bottom end (such type of ramps are called “subcritical” in the literature). And there the purely azimuthal CCF (2.5) appropriate to the local subcritical driving, $\varepsilon(z=0)$, is imposed via the boundary condition so that the amplitude of the TVF vanishes there. Most of our runs were done with quadratic ramps

$$\varepsilon(z) = \varepsilon [1 - 2(1 - z/12)^2] \quad (2.7)$$

that started at $z=0$ with $-\varepsilon$ and approached with continuous derivative the plateau, ε , at $z=12$. The axial variation of the driving with the quadratic ramp (2.7) and the resulting radial velocity in the middle of the gap is shown in Fig. 1. Some simulations were done with linear ramps

$$\varepsilon(z) = \varepsilon - 0.015(12 - z) \quad (2.8)$$

that caused a kink in the driving at the connection to the plateau. In each case the driving was constant in the plateau range $12 < z < \Gamma$ up to the top end, i.e. $\varepsilon(z > 12) = \varepsilon$.

In order to compare numerical results with theory we measure ε relative to the *numerical* bifurcation threshold for TVF which as a result of the discretization of the NSE lies slightly below the theoretical critical Reynolds number [39]. The values of $R_c^{\text{num}}(\eta=0.75) = 85.195$ and $R_c^{\text{num}}(\eta=0.893) = 126.48$ were determined by extrapolating the TVF amplitudes to zero [15] and checked against control runs with axially periodic boundary conditions [16] that avoid the Ekman vortex induced imperfect bifurcation.

The consequences of spatial ramps on dissipative structures have been discussed earlier [24–34, 10, 14]. Experimental realizations in the Taylor Couette problem were “geometrical” ramps [10, 14], where the local control parameter R was varied linearly by decreasing the gap width between the cylinders towards one end of the annulus to reach a subcritical value of the driving. Such a construction in general does not avoid the Ekman vortex at the rigid plate closing

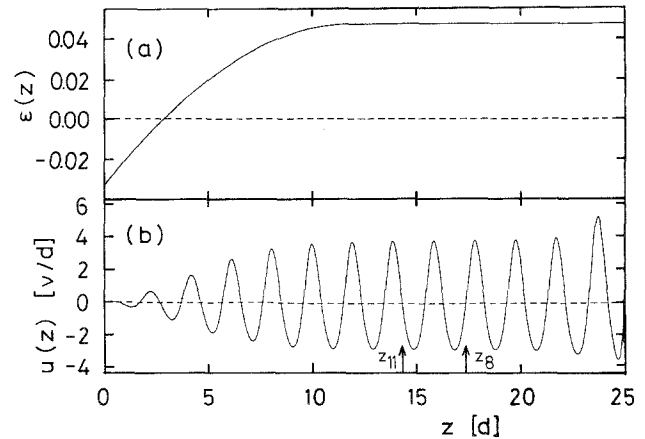


Fig. 1. **a** Spatial variation of the reduced Reynolds number with a quadratic driving ramp (2.7) ending at $z=12$ in a plateau, $\varepsilon=0.0468$. **b** Resulting stationary radial velocity field, $u(z)$, in the middle of the gap, $r=r_1 + \frac{1}{2}$ for $\eta=0.75$. Nodes of u mark axial positions of vortex centers. Maximal radial outflow (inflow) occurs at positive (negative) extrema. Except for the more intensive Ekman vortex below the stationary top plate at $z=25$ the TVF structure is uniform in the plateau range of the driving $\varepsilon(z)$. For later use some node positions z_n are indicated. Numbering starts at top end $z_0 = \Gamma = 25$

the gap, its strength is only decreased. However, our ramps together with the CCF boundary condition at $z=0$ ensure the complete absence of an Ekman vortex.

The gentle slope of the quadratic ramp enforces the TVF amplitude to decrease towards zero at $z=0$ with almost vanishing derivative and almost completely eliminates phase pinning of the TVF structure in the lower end. Thus, moving the upper plate *adiabatically* one cannot change the selected TVF structure (the wave-length can be varied only within a very narrow band – cf. Sect. 4). In fact the bulk TVF structure shows stiffness and moves together with the upper plate while faint vortices – and with it nodes in the field u shown in Fig. 1 – appear or disappear at $z=0$ (Sect. 5).

Finally we mention that ramps breaking the axial translational symmetry modify the primary CCF solution by creating large-scale vortex flow which has a bearing on the phenomena discussed in Sect. 4. Furthermore, one might expect, in particular for geometrical ramps that vortices travel in the ramp region in a way similar to those observed in conical Taylor Couette systems [40]. For the driving ramps investigated by us, this did not occur. The parameters were such that the only mechanism which could presumably enforce vortex traveling in our systems, namely selection of an unstable wave number by the ramp, was not realized (cf. Sect. 4).

3. Stationary Taylor vortices

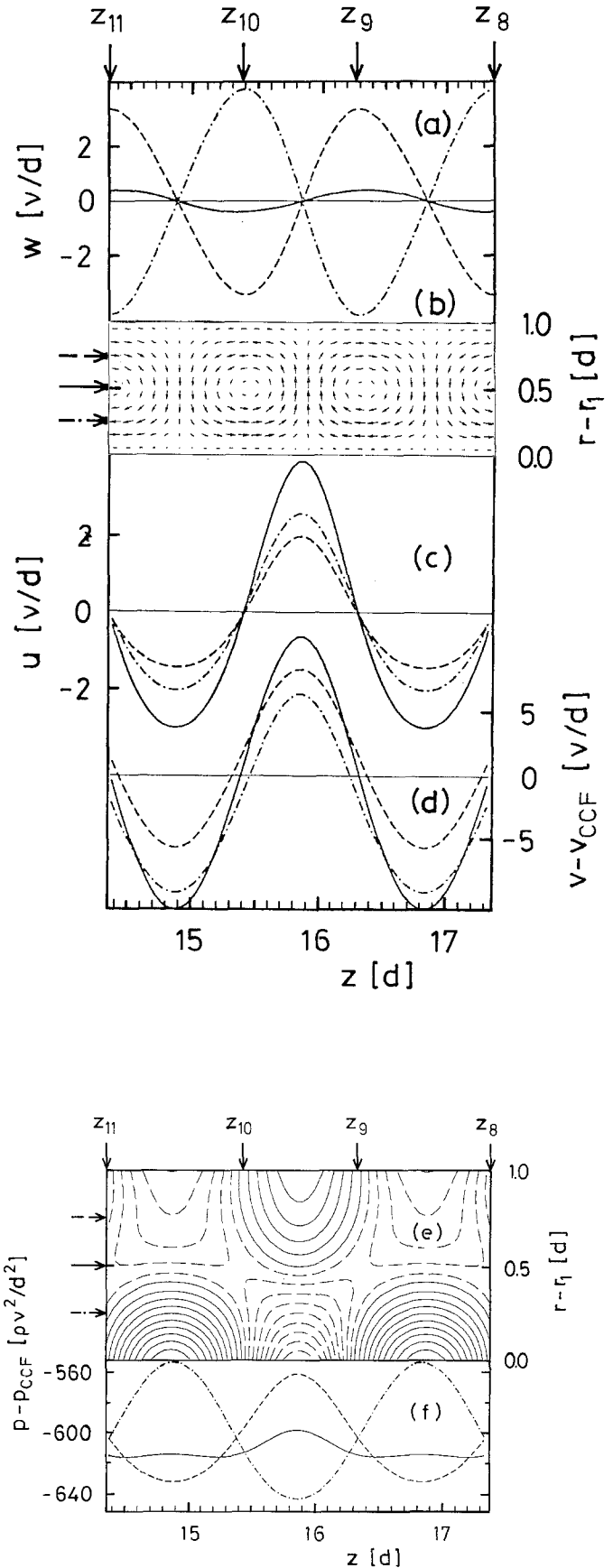
In this section we elucidate the spatial structure of Taylor vortices just above the threshold. While various details of it can be found in the literature [1, 4–23, 28, 37] we give here an overview of all fields (including the TVF part of the pressure field that so far has not been presented in detail) with a discussion of the connections between them. While Fasel and Booz [12] being primarily interested in large Reynolds number flow have given all fields some of their presentations do not easily allow to visualize the structural properties due to the TVF contribution alone.

3.1. Structure

Figure 2 shows the axial variation of the TVF structure. Note, first of all, that left and right turning vortices are mirror images of each other. The mirror planes being located at the axial positions of maximal radial inflow ($z=14.88$ and $z=16.85$) and outflow ($z=15.84$ in Fig. 2). The vortex centers are slightly displaced from the middle of the gap towards the inner cylinder, r_1 .

Although the driving is only less than 5% above the bifurcation threshold the vortices are already appreciably deformed: The asymmetry between stronger radial outflow and weaker radial inflow is most clearly seen in Fig. 2c. The origin of this asymmetry is the tangential driving by the rotation of the inner cylinder that ejects fluid radially outwards towards the stationary outer cylinder which hinders the return flow. Mass conservation then implies the axial interval $\Delta_{out}(=z_9-z_{10}=0.90$ in Fig. 2) for radial outflow to be smaller than the interval $\Delta_{in}(=z_8-z_9=z_{10}-z_{11}=1.06)$ for inflow. At threshold, $\varepsilon \rightarrow 0$, this asymmetry vanishes, $\Delta_{in}=\Delta_{out}=\lambda/2$, and outflow and inflow intensities, u_{out} and u_{in} , become identical. Here $\lambda=\Delta_{in}+\Delta_{out}$ is the wave-length. However with increasing driving the asymmetry of the flow intensities, $u_{out}-u_{in}$, increases while simultaneously Δ_{in} increases and Δ_{out} decreases relative to $\lambda/2$ (cf. below for a discussion in terms of axial Fourier modes).

Fig. 2a–f. Axial structure of TVF for the parameters of Fig. 1 in the plateau range of the driving between the positions $z_{11}=14.34$ and $z_8=17.37$ (arrows in Fig. 1) of the 11th and 8th node of u below the top plate at $z_0=\Gamma=25$. Axial velocity w (a), radial velocity u (c), azimuthal velocity $v-v_{CCF}$ (d), and pressure $p-p_{CCF}$ (f) are shown at three radial positions in the gap: $r_1+\frac{1}{4}$ (dash dotted line), $r_1+\frac{1}{2}$ (full line), and $r_1+\frac{3}{4}$ (dashed line). (b) Vector plot of the velocity field in a $r-z$ crosssection of the annulus. (e) Isolines of the pressure $p-p_{CCF}$



Also the structure of the axial velocity w can be understood from mass conservation: the axial locations of the extrema (zeros) of w coincide with the locations of the zeros (extrema) of u . Thus the above described asymmetry of u entails a sawtooth kind of deformation of w – the distance Δ_{in} between the w -extrema at z_8 and z_9 is larger than the distance Δ_{out} between the w -extrema at z_9 and z_{10} .

The extrema of the TVF induced pressure, $p - p_{CCF}$, result from stagnation and suction where the radial flow is extremal. And the extrema of u , in turn, coincide with those of the deviation $v - v_{CCF}$ of the tangential velocity v from the Couette profile – u is large (small) where v is large (small). The fact that $v - v_{CCF}$ does not vanish at the same position where $u = 0$ indicates a TVF induced zeroth axial Fourier mode, i.e. a z -independent contribution, $v_0(r)$, to v which must not be confused with the basic $v_{CCF}(r)$: the radial variation of the latter is strictly decreasing

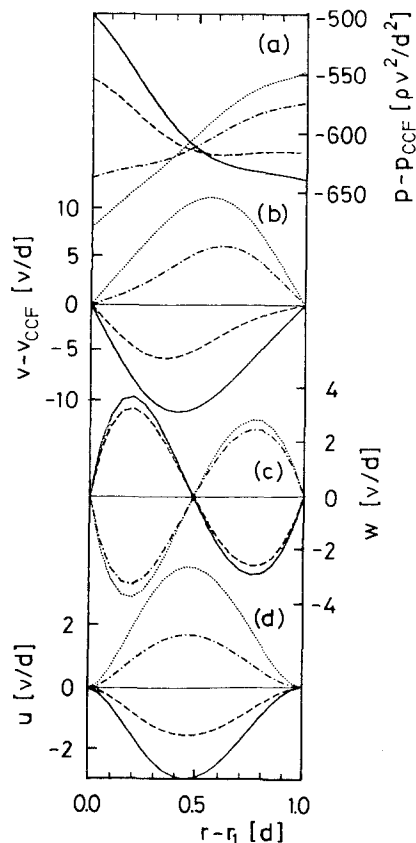


Fig. 3a-d. Radial dependence of TVF fields at different axial positions. The pressure $p - p_{CCF}$ (a), azimuthal velocity $v - v_{CCF}$ (b), and radial velocity u (d) are shown by full lines at $z = 14.85$ (maximal radial inflow), dashed lines at $z = 15.25$ (below vortex center), dash-dotted lines at $z = 15.55$ (above vortex center), and by dotted lines at $z = 15.85$ (maximal radial outflow). The axial velocity w (c) is shown by full line ($z = 15.4$) and dotted line ($z = 16.3$) where the axial flow becomes maximal. Dashed lines ($z = 15.55$) and dash-dotted lines ($z = 16.15$) show w at positions in between

while the former shows two extrema and a zero near the middle of the gap [12]. Also the pressure of the TVF contains an additional contribution $p_0(r)$ that is related to v_0 via the azimuthal momentum balance, $\partial_r p_0 = v_0^2/r$.

The structure of the axial profiles of u , w , and (to a less degree) also of $v - v_{CCF}$ is similar for each of the three radial positions included in Fig. 2 reflecting the fact that the different axial Fourier modes have similar radial dependence. This, however, does not hold for the pressure. The structure of its axial profiles differs at different radial positions (cf. lines in Fig. 2f) which can also be inferred from the isobars in Fig. 2e. We will discuss this phenomenon further below in the context of Fourier amplitudes. The pressure appears as a gradient term in the NSE and it is only fixed up to an additive constant. We have chosen the latter such that p_{CCF} vanishes at the inner cylinder.

In Fig. 3 we have put together the radial profiles of the flow at several axial positions. Here it is important to subtract the CCF part because of its dominance close to onset. The axial velocity plotted vs. r changes sign roughly at the gap center – in fact its zeros are all shifted very slightly radially inwards. Positive (negative) w implying axial upflow (downflow) occurs in a left-turning vortex in the inner (outer) half of the gap and vice versa in a right-turning vortex. Note the strong asymmetry of the axial flow intensity in the inner half of the gap and the outer half: the rotating inner (stationary outer) cylinder enhances (hinders) not only the radial flow but also the axial flow in its vicinity. Furthermore, the radial location of maximal axial flow is substantially closer to r_1 than a quarter gap width.

The asymmetry of radial outflow and inflow intensities between corresponding axial positions can be seen in Fig. 3a (dotted vs. full curve, dash-dotted vs. dashed curve). Maximal radial outflow and inflow occurs at a common radial position that is shifted from gap center towards the inner rotating cylinder.

While the profiles of u and w at different z are similar that is not the case for v and p . The reason is the TVF-induced zeroth axial Fourier mode $v_0(r)$ and $p_0(r)$, respectively. For example, adding $v_0(r)$ and the part of $v(r, z)$ that is truly oscillating in z causes at different z the total sum, v , to have different radial profiles. The radial pressure curves reflect the variations between axially alternating stagnation and suction points at the inner and outer cylinders.

3.2. Axial Fourier analysis

Having shown pictures of TVF in real space we shall now discuss its structure by an axial Fourier analysis.

The related seminal theoretical work was that of Davey [4], who evaluated the first coefficient. The subsequent Fourier analyses of experimental data obtained by Snyder and Lambert [5] (for high Reynolds numbers), Gollub and Freilich [6] (for u), Berland et al. [13] (for u), and by Heinrichs et al. [17] (for w) are critically reviewed in [17]. Numerically simulated data were presented by Fasel and Booz [12] (for v and the vorticity), Kuhlmann et al. [18] (for u and w), and in Ref. 15 (for u). In this work we have analysed all fields at a few radial positions with a standard FFT algorithm over an axial interval of 2λ in the plateau range of the ramp.

The mirror symmetry of left and right turning vortices implies relations between sine and cosine modes that we use henceforth to present our data in a more convenient form: Therein

$$u(r, \bar{z}) = \sum_{n=1}^{\infty} \hat{u}_n(r) \cos(nq\bar{z}) \quad (3.1)$$

and similarly v and p contain only cos-modes if $\bar{z}=0$ is taken to be the axial position of a mirror plane, i.e. an outflow or inflow position and the phases of all modes vanish identically. The axial velocity

$$w(r, \bar{z}) = \sum_{n=1}^{\infty} \hat{w}_n(r) \sin(nq\bar{z}) \quad (3.2)$$

contains only sine modes. Here $q=2\pi/\lambda$. According to Davey [4] the n 'th Fourier mode grows for small driving $\sim \varepsilon^{n/2}$ with a relative correction $\sim \varepsilon$.

$$\hat{u}_n(r; \varepsilon) = \varepsilon^{n/2} A_n(r) [1 + \varepsilon B_n(r)]. \quad (3.3)$$

The continuity equation, $nq\hat{w}_n = -(1/r)\partial_r(r\hat{u}_n)$, then implies analogous behavior for $\hat{w}_n(r; \varepsilon)$.

The symbols in Fig. 4 show the numerically obtained modes \hat{u}_n of the radial velocity in the middle of the gap divided by $\varepsilon^{n/2}$ for $n=1, 2, 3$. Rounding errors prohibit to present higher modes that are too small to be resolved. The dashed lines show fits to $\hat{u}_n/\varepsilon^{n/2}$ of the form $A_n(1 + \varepsilon B_n)$ supporting the validity [17] of Davey's theory [4]. The coefficients A_n and B_n of the Fourier modes of the axial velocity and the pressure (at $r=r_1 + 1/4$) were obtained in the same way. The results are compiled in Table 1. That the pressure modes \hat{p}_n have the same small- ε growth behaviour as the velocity modes \hat{u}_n, \hat{w}_n can be understood, e.g., from the axial momentum balance equation.

A direct quantitative comparison of our A_n, B_n with experimental data is made difficult by the fact that the scaling, v/d , for the latter is not given. However, we can compare quotients. The value of $A_2/A_1=0.33$

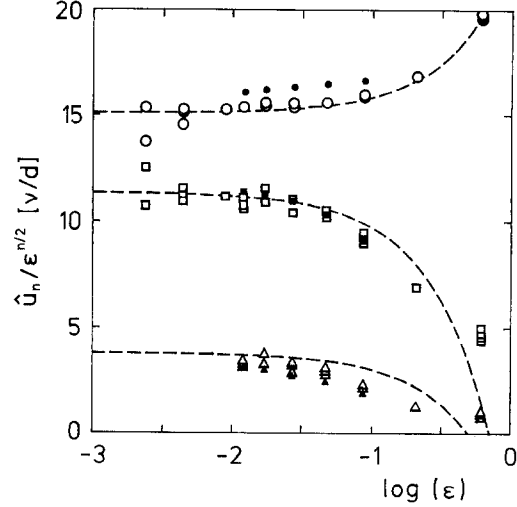


Fig. 4. ε -variation of the Fourier coefficients of u (3.1) in the middle of the gap, $r=r_1 + \frac{1}{2}$. Numerical data for $\hat{u}_n/\varepsilon^{n/2}$ obtained in the plateau region of the driving for runs with various aspect ratios, $20 \leq \Gamma \leq 25$, are denoted by circles for $n=1$, squares for $n=2$, and triangles for $n=3$. Open (full) symbols refer to radius ratio $\eta=0.75$ (0.893). Dashed lines are small- ε fits to the $\eta=0.75$ data of the form $A_n(1 + \varepsilon B_n)$ with A_n, B_n given in Table 1

Table 1. Coefficients obtained by fitting the first three numerically obtained Fourier coefficients $\hat{u}_n, \hat{w}_n, \hat{p}_n$ for small ε by $\varepsilon^{n/2} A_n(1 + \varepsilon B_n)$. The axial Fourier analysis of u, w, p is discussed in the text

	$u(r_1 + \frac{1}{2})$	$w(r_1 + \frac{1}{4})$	$p(r_1 + \frac{1}{4})$
A_1	15.2	15.8	-214
B_1	0.5	-0.07	-0.34
A_2	11.1	-6.0	26
B_2	-1.4	-2.3	4.3
A_3	3.5	1.4	-44
B_3	-2.0	-0.25	-1.3

reported in [14, 17] for the axial velocity agrees well with our 0.38. Their first corrections $B_1=0.06$, $B_2=-1$ compare not so well with our $B_1=-0.07$, $B_2=-2.3$. The data of Berland et al. [13] for the radial velocity are $A_2/A_1=0.45$ vs. our 0.73 and $A_3/A_1=0.10$ vs. our 0.23. Also their correction terms disagree with ours.

The Fourier modes $\hat{u}_n(r)$ (and also $\hat{w}_n(r)$) have for different n similar radial profiles [12] resembling the shapes given in Fig. 3d(3c). That does not hold for the pressure: the radial variation of $\hat{p}_n(r)$ is for different n quite different as shown in Fig. 5. The first mode $\hat{p}_1(r)$ has a shape similar to that of the entire pressure like in Fig. 3a. Since the second and third modes become dominant when $\hat{p}_1(r)$ has a zero their contribution can be seen in the solid curve of Fig. 2e.

Finally we contrast some of the structural properties of toroidal, closed Taylor vortices with those of

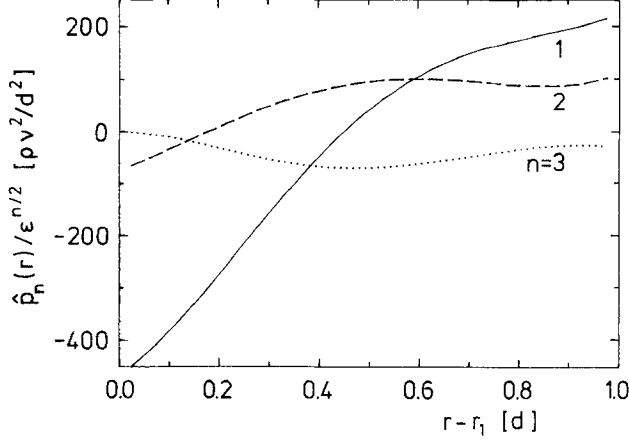


Fig. 5. Radial dependence of the axial Fourier modes $\hat{p}_n(r)$ of the pressure field ($\eta=0.75$, $\varepsilon=0.0468$)

straight, parallel roll vortices arising in Rayleigh-Bénard convection (RBC) of a horizontal fluid layer heated from below. We compare the $r-z$ crosssection of TVF with the vertical section perpendicular to the roll axes of the RBC layer and radial and axial velocity components of TVF with vertical and horizontal components in RBC, respectively. In both systems stationary left and right turning vortices are mirror images of each other. However, while in RBC vertical up- and downflow intensities between adjacent roll vortices are practically the same [41] there is in the TVF case already for small ε a strong asymmetry between maximal out- and inflow intensities, u_{out} and u_{in} . For small ε one finds from (3.1, 3.3)

$$u_{\text{out}} = \sqrt{\varepsilon} A_1 \left[1 + \sqrt{\varepsilon} \frac{A_2}{A_1} + \varepsilon \left(B_1 + \frac{A_3}{A_1} \right) \right] + 0(\varepsilon^2) \quad (3.4)$$

$$u_{\text{in}} = \sqrt{\varepsilon} A_1 \left[1 - \sqrt{\varepsilon} \frac{A_2}{A_1} + \varepsilon \left(B_1 + \frac{A_3}{A_1} \right) \right] + 0(\varepsilon^2) \quad (3.5)$$

so that, e.g., for $\varepsilon=0.01$ the ratio of $u_{\text{out}}/u_{\text{in}}$ has grown already to 1.15. Simultaneously the node distances of u

$$\Delta_{\text{out}} = \frac{\lambda}{2} - \sqrt{\varepsilon} \frac{\lambda}{\pi} \frac{A_2}{A_1} \left\{ 1 - \varepsilon \left[B_1 - B_2 + \frac{11}{6} \left(\frac{A_2}{A_1} \right)^2 - 3 \frac{A_3}{A_1} \right] \right\} + 0(\varepsilon^2) \quad (3.6)$$

$$\Delta_{\text{in}} = \lambda - \Delta_{\text{out}} \quad (3.7)$$

differ already by a factor of $\Delta_{\text{in}}/\Delta_{\text{out}}=1.05$ with $\lambda=2.0$. Note that this asymmetry of TVF which is related to the large size of A_2 severely limits the range of applicability of the lowest-order amplitude Eq. [2] that takes into account only the $n=1$ mode. For the more symmetric RBC the weakly-nonlinear perturba-

tion expansion around threshold holds up to larger driving [41].

RBC breaks for small ε only very weakly the mid-plane mirror symmetry at half height of the layer that the governing hydrodynamic equations possess while a midgap symmetry of the NSE for TVF does not exist – the inner rotating cylinder is also in the equation for the secondary TVF singled out against the outer stationary one. And finally, the roll vortex flow of stationary RBC is invariant under a combination of a vertical mirror operation at midheight combined with a horizontal translation by $\lambda/2$ [41]. TVF, on the other hand, shows no sign of this symmetry.

4. Wavenumber selection

In this section we discuss the question which wavelengths are realized in our ramped system. In the last years this problem of structure selection was treated in various theoretical [24–33] and experimental [10, 14, 34] investigations. Kramer et al. [25] demonstrated for a set of reaction-diffusion equations that smooth ramps with subcritical control parameters at one end lead to an unique wave number $q(\varepsilon)$ of the dissipative structure. The selected wave number is independent of ramps shape as long as only one parameter is varied to build it up and the axial variation is sufficiently smooth. But ramps, $\varepsilon(z)$, caused by a variation of different parameters (e.g. d or v_1) can select different wave numbers. Pomeau and Zaleski [26] got for a special amplitude equation near threshold a linear shift of the selected $q(\varepsilon)$ from the critical wave number q_c [1]. The slope $\partial q(\varepsilon)/\partial$ is determined by the coefficients of the amplitude equation. The behavior of $q(\varepsilon)$ for larger ε , however, can only be calculated with the theory of Ref. 25.

The experiments of Ahlers et al. [10, 14], on the other hand, show a narrow band of possible wave numbers in the presence of a ramp. This can be traced back [29, 32] to the existence of phase pinning caused by deviations from the smoothness in the transition region between the linear ramp and the bulk supercritical plateau for example the step in the first derivative of the control parameter. The resulting pinning center influences the wavenumber selection in two ways: First via a large-scale z -dependent flow of small intensity that yields a divergence $\Delta q = a/\sqrt{\varepsilon}$ of the band width [29, 32] called the anomalous band. This behaviour of the band of possible wave numbers can be well seen in the experiments [10, 14], but the prefactor a is not proportional to the slope of the ramp as suggested in [29]. On the other hand in the high- ε regime, when the large-scale flow can be neglected, the pinning center leads to an ε -independent band width [32] called normal band. Riecke [32] calculat-

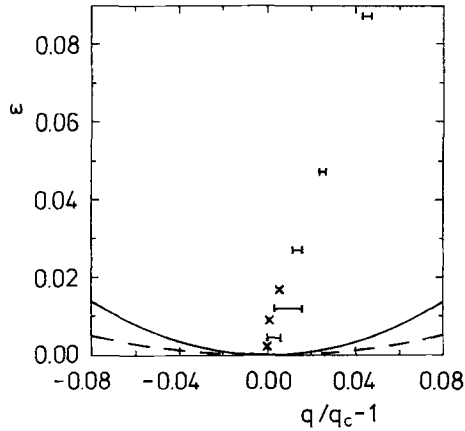


Fig. 6. Wave number band for the quadratic driving ramp (2.7) vs. control parameter ε . Bars indicate the observed range for $\eta = 0.75$. A cross is plotted for ε -values for which too few simulation data are available. Below the full line, $\varepsilon_B = 3\xi_0^2(q - q_c)^2$, TVF is unstable against the Eckhaus instability [45]. The dashed line, $\varepsilon_m = \xi_0^2(q - q_c)^2$, is the marginal stability curve of CCF above which the latter is unstable. $\xi_0 = 0.27$, $q_c = 3.135$ [35]

ed a value of $\Delta q/q_c = \frac{\alpha}{8}$ for the normal band where α denotes the slope of the linear ramp. Also this band behaviour can be seen in the experiments. For $\alpha = 0.03$ the experimental data agree very well with $\Delta q/q_c = \frac{\alpha}{8}$, while for $\alpha = 0.015$ the experimental band is smaller than predicted. But for both slopes of the experimental ramps the width was constant in a wide ε -region.

In our numerical simulation we performed two runs with a linear driving ramp of angle $\alpha = 0.015$. At $\varepsilon = 0.047$ our band width Δq is the same as the experimental one [14] with the geometrical ramp. But for $\varepsilon = 0.087$ our width is almost twice the experimental one. Furthermore the center of our wavenumber band is in both cases shifted to higher q . These differences between the numerical and experimental results might reflect the fact that for our driving ramp the gap is constant. Furthermore there are no geometrical imperfections in our system that necessarily arise in experiments with geometrical ramps, e.g. where the conically shaped annulus joins the cylindrical region.

In Fig. 6 we show the wave numbers as a function of ε that are realized in our setups with various different aspect ratios $20 \leq \Gamma \leq 25$ and with the *quadratic* driving ramp (2.7) in the lower part of the annulus. For each Γ the wave-length of the stationary TVF structure in the middle of the plateau range of the driving between $z = 12$ and $z = \Gamma$ was evaluated. For our smooth quadratic ramp that resembles more the idealized situation considered in the theory, we observe a strong contraction of the band width compared to a corresponding linear ramp. The contrac-

tion is almost a factor 7 for those quadratic ramps that have near their zerocrossing, $\varepsilon(z) = 0$, roughly the slopes of the two linear ramps investigated by us.

Riecke has evaluated the band width in the Swift-Hohenberg model [32] for ramps, $\varepsilon(z) = \varepsilon + \frac{\alpha}{2}z$ $\cdot \left[1 - \frac{\zeta}{z} \ln\left(2 \cosh \frac{z}{\zeta}\right)\right]$, that show a smooth crossover over a distance ζ from linear behaviour with slope α at $z \rightarrow -\infty$ to a plateau of height ε at $z \rightarrow +\infty$. But a comparison is questionable since Riecke's result pertain to a model equation, since his ramp structure differs from ours, and since our ramp is always by construction in the crossover region from normal to anomalous band.

Finally we discuss the position of the center of the band of selected wave numbers. This band center position, $q^*(\varepsilon)$, is practically the same for our linear and quadratic ramps in agreement with the prediction of [25]. Furthermore, it varies for small ε linearly with ε which is consistent with [25, 26].

5. Phase dynamics

Here we study the phase dynamics of the TVF structure, e.g., the dynamics of the nodes of the radial velocity field and in particular its long-time diffusive behaviour when approaching the stationary final state.

The concept of describing the phase dynamics of patterns by phase diffusion equations is very general [42–44]. Tabeling [21] has analyzed older experiments by Snyder [20] using this concept. Riecke has derived [23] a diffusion equation directly from the NSE and has compared for several ε and q has diffusion constants with experimental data of Gerdtts [22]. Another method for describing the phase dynamics is to use weakly nonlinear perturbation theory around the bifurcation threshold $\varepsilon = 0$. Within this approach the radial velocity field solving the NSE to lowest order in $\sqrt{\varepsilon}$ has the form [2]

$$u(r, z, t) = \text{Re}[A(z, t) e^{iq_c z} u^{(1)}(r)]. \quad (5.1)$$

Here q_c is the critical wave number, $u^{(1)}(r)$ is the radial eigenfunction of the linear problem at threshold and

$$A(z, t) = R(z, t) e^{i\phi(z, t)}; \quad R = |A| \quad (5.2)$$

is the axially and temporally slowly varying complex amplitude function of the flow bifurcating from the CCF state. According to Eagles and Eames [27, 30] the equation determining A differs from the standard

Ginzburg-Landau amplitude equation (3)

$$[\tau_0 \partial_t - \xi_0^2 \partial_z^2 - \varepsilon + g|A|^2] A = 0 \quad (5.3)$$

by the fact that a z -dependent, real function appears which contains among others the ramping function $\varepsilon(z)$. However the resulting equation for the phase $\phi(z, t)$

$$R^2 \partial_t \phi = D_0 \partial_z [R^2 \partial_z \phi] \quad (5.4a)$$

is the same as for the standard unramped case. Here

$$D_0 = \xi_0^2 / \tau_0 \quad (5.4b)$$

is the diffusion constant in an ideal system where $A(z, t \rightarrow \infty)$ approaches a z -independent constant. With $\xi_0 = 0.2694$ and $\tau_0 = 0.03796$ for $\eta = 0.75$ following from a linear stability analysis of the CCF [35] the phase diffusion constant in the ideal reference system is $D_0 = 1.912$. Note that whenever the amplitude R of the TVF state shows an axial variation then the phase dynamics is not purely diffusive (cf. below).

In our numerical simulations we studied the dynamics of the response of the TVF structure to a variation of the annulus length [22]. Starting from a stationary TVF state in a system of initial aspect ratio Γ_i we moved the top plate with constant speed to various final values Γ_f . Typically the change in Γ was $0.2 \leq \Delta\Gamma \leq 1$. The resulting evolution of the flow fields towards the stationary TVF state appropriate to Γ_f was then monitored. Figure 7 shows the world-lines of the node positions, $z_n(t)$, of the radial velocity field in the middle of the gap, i.e., of the vortex centers for a typical situation with a quadratic ramp when

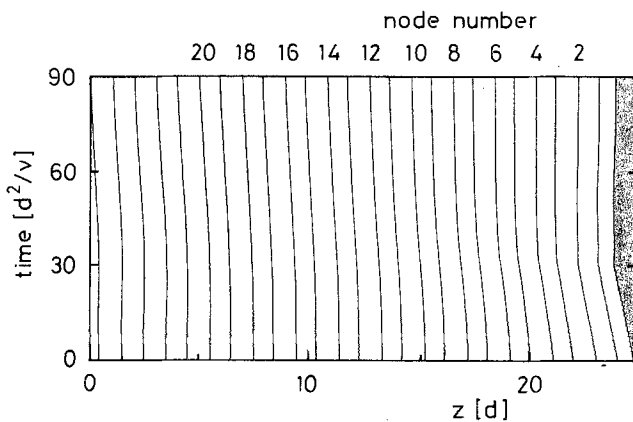


Fig. 7. Time evolution of vortex positions. World lines of all nodes of the radial velocity in the middle of the gap are shown when the upper plate $z_0(t) = \Gamma(t)$ is moved downwards by 1 (in 20 steps of the numerical discretization length). The initial state is the stationary TVF of Fig. 1 with quadratic ramp. After the downwards motion of the vortices (one is expelled at $z=0$ with zero intensity) the structure of the shifted TVF state is identical to the initial one except for the ramp region

Γ was decreased by 1 with speed 1/30. The initial state was the one for which u is shown in Fig. 1. The final state is almost identical to the initial one, albeit shifted axially by 1. Superimposing the radial velocity fields of the initial flow and the final axially shifted state one verifies that they coincide except near the bottom end. There the phase, i.e., the node positions have adjusted such as to accommodate the same structure in the bulk. Thus the vortices follow the downward motion of the top plate and eventually a vortex with vanishing amplitude is annihilated at $z=0$ – a node is pushed out there.

The world lines reveal a fast non diffusive initial response of vortices close to the moving top plate which cannot be described within the amplitude equation approach for slow processes. For example, the 20 small steps in the world line $z_1(t)$ of the first vortex center below the top boundary reflect an instantaneous reaction to the motion of the boundary – the latter is moved (from $\Gamma_i=25$ to $\Gamma_f=24$ in Fig. 7) in discrete steps about every radial diffusion time by $\Delta z = 1/20$ which is our numerical discretization length. This fast, almost rigid-like motion is the result of the incompressibility constraint: pressure variations and with it the resulting forces on the velocity field are felt instantaneously over the whole system with an intensity that decreases axially from the top plate.

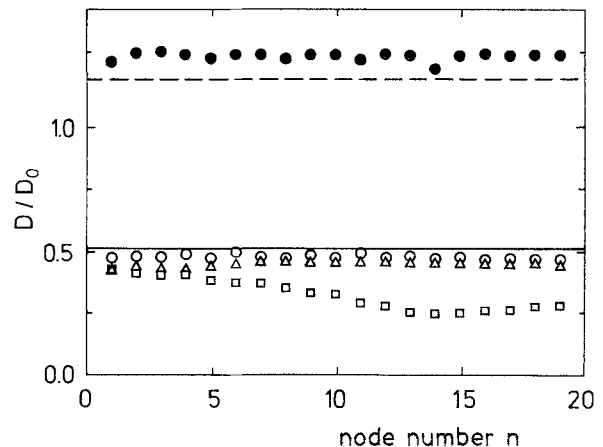


Fig. 8. Reduced phase diffusion constants. Symbols result from the long-time relaxation of vortex centers – node positions $z_n(t)$ of the radial velocity field in the middle of the gap – after moving the top plate downwards by $\Delta\Gamma = 0.2$. Full dots refer to case (i): constant driving profile with two rigid endplates. Circles and triangles represent case (ii): quadratic driving ramp (2.7). Triangles come from control run with $\Delta\Gamma = 1$. Squares denote case (iii): linear driving ramp (2.8). In all cases $\eta = 0.75$, $\varepsilon = 0.047$, and initial $\Gamma = 25$. Lines (dashed one for case i and full one for case ii) result from phase Eq. (5.4) using the numerically obtained amplitude profiles (Fig. 9) as input (cf. text for details)

The long-time motion of the vortex centers $z_n(t)$ towards their final positions $z_n(\infty)$, however, is a slow relaxation process

$$z_n(t) - z_n(\infty) \sim e^{-\gamma_n t} \quad (5.5)$$

whereas the adjustment of the vortex amplitudes is a relatively fast process. The relaxation rates γ_n that we determined by proper fits to $z_n(t)$ are almost independent of the node position as shown in Fig. 8. There we compare our numerically observed relaxation rates with results from the phase Eq. (5.4) of the weakly nonlinear theory. To that end we relate [43] the relaxation rates γ of the nodes to the phase diffusion constant D via

$$D = \frac{\pi^2}{\Gamma^2} \gamma. \quad (5.6)$$

According to (5.1) the rate of change $\dot{z}_n(t)$ of a node position is given by $-\partial_t \phi / (q_c + \partial_z \phi)$ evaluated at z_n .

We present in Fig. 8 the results for (i) two rigid endplates with a constant driving profile – full dots, (ii) quadratic ramps (2.7) – circles and triangles, and (iii) linear ramp (2.8) – squares. In each case the bulk driving was $\varepsilon = 0.047$ and the top plate was moved downwards by $\Delta\Gamma = 0.2$. In the unramped system we moved top and bottom boundaries simultaneously by 0.2 to guarantee the same final state. The open circles for the quadratically ramped system were obtained from a control run with $\Delta\Gamma = 1$. In the unramped system the diffusion constant is clearly larger (in almost quantitative agreement with experimental [22] and theoretical [23] results) than in the ideal reference system while in the presence of a linear or quadratic ramp it is smaller by almost a factor of two. These deviations are caused by the particular z -dependent amplitude profiles of the TVF states in these systems as well shall now explain with the phase Eq. (5.4).

For the long-time behaviour of the phase we can ignore the time dependence of the amplitude and use the final profile $R(z)$. Consider the deviation

$$\varphi(z, t) = \phi(z, t) - \phi(z, t = \infty) \quad (5.7)$$

from the final stationary phase. The latter solves $\partial_z [R^2(z) \partial_z \phi(z, t = \infty)] = 0$ with the appropriate boundary conditions and thus is determined by the amplitude profile [37]. Expanding φ in terms of sine-functions

$$\varphi(z, t) = \sum_{n=1} \varphi_n(t) |n\rangle; \quad |n\rangle = \sqrt{(2/\Gamma)} \sin(n\pi z/\Gamma) \quad (5.8)$$

the partial differential equation

$$R \partial_t \varphi = D_0 [R \partial_z^2 + 2(\partial_z R) \partial_z] \varphi$$

is transformed into an infinite dimensional system of ordinary differential equations

$$S_{nm} \dot{\varphi}_m(t) = -D_0 \left(\frac{\pi}{\Gamma}\right)^2 T_{nm} \varphi_m(t). \quad (5.9)$$

The matrices

$$S_{nm} = \langle n | R | m \rangle = R_{n-m} - R_{n+m} \quad (5.10)$$

$$T_{nm} = -\left(\frac{\Gamma}{\pi}\right)^2 \langle n | R \partial_z^2 + 2(\partial_z R) \partial_z | m \rangle = m^2 S_{nm} + 2m[(n-m)R_{n-m} + (n+m)R_{n+m}] \quad (5.11)$$

are given in terms of cos-modes of $R(z)$

$$R_j = \frac{1}{\Gamma} \int_0^\Gamma dz \cos\left(j\pi \frac{z}{\Gamma}\right) R(z). \quad (5.12)$$

The eigenvalues of $S^{-1}T$ are positive thus enforcing $\varphi_n(t \rightarrow \infty) = 0$ and the smallest one governs the exponential long-time decay of φ . In the ideal reference system where $R = \text{const} = R_0$ and $R_n = 0$ for $n \neq 0$ the j -th eigenvalue is $\lambda_j = j^2$ with $\lambda_1 = 1$ leading to a diffusion constant D_0 . For any $R(z)$ profile that contains higher cos-contributions the smallest eigenvalue and with it the diffusion constant will be changed. The mechanism can be seen already in the most drastic truncation of the infinite dimensional matrices to their

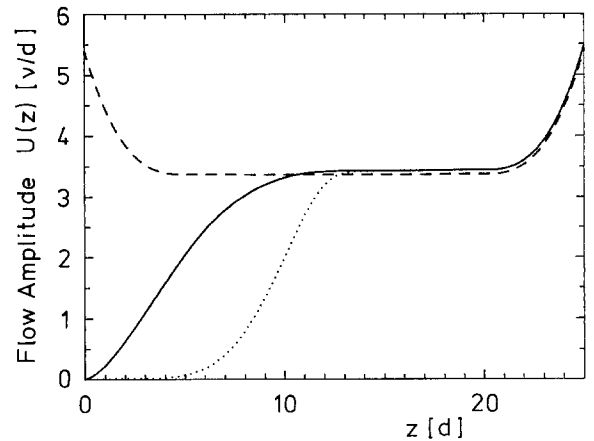


Fig. 9. TVF amplitude profiles resulting from the arithmetic mean of the spline fitted envelopes of radial inflow and outflow extrema in the middle of the gap. Dashed line (i) -constant driving with two stationary endplates, full line (ii) -quadratic driving ramp, dotted line (iii) -linear driving ramp. The slightly smaller plateau height of the dashed profile is due to a different wave number in case (i). In each case $\eta = 0.75$, $\varepsilon = 0.047$ with a rigid top plate at $\Gamma = 25$ causing the Ekman enhancement of the amplitude profile in its vicinity

1,1 element. That yields

$$\frac{D}{D_0} = \frac{R_0 + 3R_2}{R_0 - R_2}. \quad (5.13)$$

To be more specific we identify the profile of $R(z)$ – scaling factors drop out – with the function $U(z)$ shown in Fig. 9

$$R(z) \leftrightarrow U(z). \quad (5.14)$$

It was determined from our numerical simulations by making separate spline fits through the outflow and inflow extrema of the radial velocity in the middle of the gap. The arithmetic mean of the resulting two envelopes is taken as a representative amplitude function, $U(z)$, of the TVF state.

Note first in Fig. 9 the Ekman vortex enhancement of the amplitude profile at the top plate common to all cases (i)–(iii) and the plateau region of constant amplitude between $z=12$ and, say, 22. In the lower part of the annulus $U(z)$ shows without a ramp (dashed line) the Ekman enhancement as well. The amplitude drops rather rapidly to zero (dots) in the presence of the linear ramp (2.8) and more slowly (full line) for the quadratic ramp (2.7) – the former is steeper and drops to smaller subcritical driving than the latter. From approximation (5.13) it becomes clear that in the ramped systems the diffusion constant is smaller than D_0 while it is enhanced for the dashed line profile in the standard unramped setup: the contribution from the second cos-mode to the amplitude profile $R_2/R_0 = U_2/U_0$ is positive (~ 0.06) for the dashed line while it is negative (~ -0.1) for the full and the dotted line representing the ramped systems. Thus the approximation (5.13) yields a diffusion constant that is in the unramped system enhanced (by $\sim 25\%$) and reduced (by $\sim 36\%$) in the ramped systems. As an aside we remark that one can understand with (5.13) also the reduction of the phase diffusion constant of the standard convective roll pattern in the Rayleigh-Bénard system seen in the experiments of Croquette and Schosseler [43]: since the convective amplitude profile drops to zero on both ends of the experimental container R_2 is negative.

For a more quantitative treatment of the phase diffusion equation we truncated the matrices at increasing order N . Plotting the smallest eigenvalue of $S^{-1}T$ versus $1/N$ we determined the $N \rightarrow \infty$ limit. To do so, we used only U_n for $n \leq 6$ and set $U_{n>6} = 0$. The resulting diffusion constants are shown in Fig. 8 by a dashed line for the unramped system and a full line for the system with quadratic ramp. One should keep in mind that in order to have such a good agreement between the phase Eq. (5.4) from lowest-order perturbation theory and the numerical simulation of

the full NSE one has to use the correct amplitude profile from the full equations.

The initial part of this work was done at the Institut für Festkörperforschung, KFA Jülich. Its support, the numerical assistance by M. Kamps, B. Kowalski, K. Wingerath, and discussions with M. Mihelečić are gratefully acknowledged. This work was supported by the Volkswagen-Stiftung.

References

1. DiPrima, R.C., Swinney, H.L.: In: Hydrodynamic instabilities and transition to turbulence, p. 139. Swinney, H.L., Gollub, J.P. (eds.), Berliia, Heidelberg, New York: Springer 1985
2. Yahata, H.: Progr. Theoret. Phys. **57**, 347, 1490 (1977); Graham, R., Domaradzki, J.A.: Phys. Rev. A **26**, 1572 (1982)
3. Newell, A.C., Whitehead, J.A.: J. Fluid Mech. **38**, 279 (1969); Segel, L.A.: ibid. **38**, 203 (1969)
4. Davey, A.: J. Fluid Mech. **14**, 336 (1962)
5. Snyder, H.A., Lambert, R.B.: J. Fluid Mech. **26**, 545 (1966)
6. Gollub, J.P., Freilich, M.H.: Phys. Fluids **19**, 618 (1976)
7. Majumdar, A.K., Spalding, D.S.: J. Fluid Mech. **81**, 295 (1977)
8. Meyer-Spasche, R., Keller, H.: J. Comp. Phys. **35**, 100 (1980)
9. Pfister, G., Rehberg, I.: Phys. Lett. **83A**, 19 (1981)
10. Cannell, D.S., Dominguez-Lerma, M.A., Ahlers, G.: Phys. Rev. Lett. **50**, 1365 (1983); Dominguez-Lerma, M.A., Cannell, D.S., Ahlers, G.: Phys. Rev. A **34**, 4956 (1986)
11. Lücke, M., Mihelečić, M., Wingerath, K.: Phys. Rev. Lett. **52**, 625 (1984); Phys. Rev. A **31**, 396 (1985)
12. Fasel, H., Booz, O.: J. Fluid Mech. **138**, 21 (1984)
13. Berland, T., Jøssang, T., Feder, J.: Phys. Scr. **34**, 427 (1986)
14. Ahlers, G., Cannell, D.S., Dominguez-Lerma, M.A., Heinrichs, R.: Physica **23D**, 202 (1986)
15. Lücke, M., Mihelečić, M., Kowalski, B., Wingerath, K.: In: The physics of structure formation: Theory and simulation, p. 97. Güttinger, W., Dangelmayr, G. (eds.). Berlin, Heidelberg, New York: Springer 1987; Verh. DPG (VI) **21**, 1052 (1986)
16. Roth, D.: Diplomarbeit. Saarbrücken, 1988 (unpublished)
17. Heinrichs, R.M., Cannell, D.S., Ahlers, G., Jefferson, M.: Phys. Fluids **31**, 250 (1988)
18. Kuhlmann, H., Roth, D., Lücke, M.: Phys. Rev. A **39**, 745 (1989)
19. Ahlers, G.: In: Complex systems, SFI studies in the sciences of complexity. Stein, D. (ed.). Amsterdam: Addison Wesley 1989
20. Snyder, H.A.: J. Fluid Mech. **35**, 273 (1969)
21. Tabeling, P.: J. Phys. (Paris) Lett. **44**, L665 (1983)
22. Gerdtts, U.: PhD thesis. Kiel, 1985 (unpublished)
23. Riecke, H.: PhD thesis. Bayreuth, 1986 (unpublished)
24. Eagles, P.M.: Proc. R. Soc. London Ser. A **371**, 359 (1980)
25. Kramer, L., Ben-Jacob, E., Brand, H., Cross, M.C.: Phys. Rev. Lett. **49**, 1891 (1982)
26. Pomeau, Y., Zaleski, S.: J. Phys. (Paris) Lett. **44**, L135 (1983)
27. Eagles, P.M., Eames, K.: J. Eng. Math. **17**, 263 (1983)
28. Lücke, M.: In: Summary of the proceedings of the sixtieth anniversary Taylor vortex flow workshop, June 1983, Eugene, Oregon. Park, K., Donnelly, R.J. (eds.) (unpublished)
29. Cross, M.C.: Phys. Rev. A **29**, 391 (1984)
30. Eagles, P.M.: Phys. Rev. A **31**, 1955 (1985)
31. Kramer, K., Riecke, H.: Z. Phys. B – Condensed Matter **59**, 245 (1985); Buell, J.C., Catton, I.: J. Fluid Mech. **171**, 477 (1986)

32. Riecke, H.: *Europhys. Lett.* **2**, 1 (1986); *Phys. Rev. A* **37**, 636 (1988)
33. Riecke, H., Paap, H.-G.: *Phys. Rev. Lett.* **59**, 2570 (1987)
34. Rehberg, I., Bodenschatz, E., Winkler, B., Busse, F.H.: *Phys. Rev. Lett.* **59**, 282 (1987);
Rehberg, I., Riecke, H.: In: *The physics of structure formation: Theory and simulation*, p. 142.
Güttinger, W., Dangelmayr, G. (eds.). Berlin, Heidelberg, New York: Springer 1987
35. Dominguez-Lerma, M.A., Ahlers, G., Cannell, D.S.: *Phys. Fluids* **27**, 856 (1984)
36. Hirt, C.W., Nichols, B.D., Romero, N.C.: Los Alamos Scientific Laboratory Report No. LA-5652, 1975 (unpublished)
37. Heinrichs, R., Ahlers, G., Cannell, D.S.: *Phys. Rev. Lett.* **56**, 1794 (1986)
38. Niklas, M.: PhD thesis. Aachen, 1988 (unpublished);
Niklas, M., Lücke, M., Müller-Krumbhaar, H.: *J. Magn. Magn. Mater.* **81**, 29 (1989)
39. In Ref. 11 ε is measured relative to the *theoretical* bifurcation threshold R_c .
40. Wimmer, M.: *Prog. Aerospace Sci.* **25**, 43 (1988);
Abboud, M., *ZAMM* **68**, T275 (1988)
41. Niederländer, J., Lücke, M., Kamps, M.: (unpublished)
42. Pomeau, Y., Manneville, P.: *J. Phys. (Paris) Lett.* **40**, L609 (1979)
43. Wesfreid, J.E., Croquette, V.: *Phys. Rev. Lett.* **45**, 634 (1980);
Croquette, V., Schosseler, F.: *J. Phys. (Paris)* **43**, 1183 (1982)
44. Brand, H.R.: In: *Propagation in systems far from equilibrium*, p. 206.
Wesfreid, J.E., Brand, H.R., Manneville, P., Albinet, G., Boccara, N. (eds.). Berlin, Heidelberg, New York: Springer 1988, and references cited therein
45. Eckhaus, W.: *Studies in nonlinear stability theory*. Berlin, Heidelberg, New York: Springer 1965

M. Lücke, D. Roth
 Institut für Theoretische Physik
 Universität des Saarlandes
 D-6600 Saarbrücken
 Federal Republic of Germany